



**HAL**  
open science

## High-Temperature Deformation Behavior of 718Plus: Consideration of $\gamma'$ Effects

Utkudeniz Ozturk, Jose Maria Cabrera, Jessica Calvo, Abdelkrim Redjaïmia,  
Jaâfar Ghanbaja

► **To cite this version:**

Utkudeniz Ozturk, Jose Maria Cabrera, Jessica Calvo, Abdelkrim Redjaïmia, Jaâfar Ghanbaja. High-Temperature Deformation Behavior of 718Plus: Consideration of  $\gamma'$  Effects. *Materials Performance and Characterization*, 2020, Peculiarities of Microstructure Evolution and Property Changes of Titanium Alloys In Situ during Electric Forging, 9 (2), pp.57-74. 10.1520/mpc20190031 . hal-04316632

**HAL Id: hal-04316632**

**<https://hal.univ-lorraine.fr/hal-04316632>**

Submitted on 30 Nov 2023

**HAL** is a multi-disciplinary open access archive for the deposit and dissemination of scientific research documents, whether they are published or not. The documents may come from teaching and research institutions in France or abroad, or from public or private research centers.

L'archive ouverte pluridisciplinaire **HAL**, est destinée au dépôt et à la diffusion de documents scientifiques de niveau recherche, publiés ou non, émanant des établissements d'enseignement et de recherche français ou étrangers, des laboratoires publics ou privés.

Utkudeniz Ozturk,<sup>1</sup> Jose Maria Cabrera,<sup>2</sup> Jessica Calvo,<sup>2</sup> Abdelkrim Redjaïmia,<sup>3</sup> and Jaâfar Ghanbaja<sup>3</sup>

## High-Temperature Deformation Behavior of 718Plus: Consideration of $\gamma'$ Effects

### Reference

U. Ozturk, J. M. Cabrera, J. Calvo, A. Redjaïmia, and J. Ghanbaja, "High-Temperature Deformation Behavior of 718Plus: Consideration of  $\gamma'$  Effects," *Materials Performance and Characterization* 9, no. 2 (2020): 57–74. <https://doi.org/10.1520/MPC20190031>

### ABSTRACT

The hot deformation behavior of 718Plus is modeled through a physically based hybrid dislocation density model, which includes the effects of precipitating particles. It is well known that the service performance and hot flow characteristics of this alloy are strongly dependent on the microstructure, particularly the grain size and second-phase particles. Thus, comprehension and modeling of the hot flow behavior is an important task. In precipitation hardening alloys (superalloys, microalloyed steels, etc.), it is particularly challenging to model the microstructural evolution in the processing windows, where material softening and precipitation processes take place concurrently. In this work, the initial stages of the deformation are studied. A model based on dislocation density evolution is presented. As in conventional approaches, the dislocation density is considered as a competition between dislocation generation and dynamic recovery at the early stages of deformation. Recovery is assumed to be driven by glide and climb of dislocations, which are considered to be proportional to the strain rate and damped by the existence of second-phase particles. It is known that under high-temperature deformation conditions, 718Plus may undergo dynamic precipitation. Second-phase particles in the material may impede the grain boundary motion and contribute to an increase in flow stress. To account for the dynamic precipitation, the present model combines experimental results and precipitation models to predict volume fraction and particle size. The effect of aging is studied through transmission electron microscopy (TEM) characterization of the specimens from interrupted tests at the onset of dynamic recrystallization. Stress contribution due to different modes of dislocation precipitation interaction are modeled and integrated to the phenomenological dislocation density-based hardening models.

### Keywords

superalloy 718Plus, hot forming, hot flow behavior, hot flow modeling, precipitation strengthening, dynamic precipitation, gamma prime, effect of gamma prime on hot flow behavior

Manuscript received January 31, 2019; accepted for publication October 14, 2019; published online January 16, 2020. Issue published July 27, 2020.

<sup>1</sup> Departamento de Ciencia de los Materiales e Ingeniería Metalúrgica, Universitat Politècnica de Catalunya (EEBE – UPC), Eduard Maristany 10-14 Barcelona, Catalunya 08930, Spain (Corresponding author), e-mail: [utkudenizozturk@gmail.com](mailto:utkudenizozturk@gmail.com), <https://orcid.org/0000-0002-7854-8442>

<sup>2</sup> Departamento de Ciencia de los Materiales e Ingeniería Metalúrgica, Universitat Politècnica de Catalunya (EEBE – UPC), Eduard Maristany 10-14 Barcelona, Catalunya 08930, Spain

<sup>3</sup> Université de Lorraine, Institut Jean Lamour, Laboratoire d'Excellence, CNRS UMR 7198, Nancy 54011, France, <https://orcid.org/0000-0003-2413-1470> (A.R.)

## Introduction

Inconel 718Plus was introduced in early 2000s to respond the needs of increasing service temperatures while keeping the manufacturing costs moderate. Inconel 718Plus presents a 50°C higher temperature capability over its ancestor Inconel 718.<sup>1</sup> The chemical compositions of both alloys are given in **Table 1**.

The hot workability and the effect of processing routes on the final service performance of the alloy are important areas of investigation, especially for the recently developed alloys. Regarding the hot working of 718Plus, the literature is still in development. In contrast, its predecessor Inconel 718 is well studied, and a high number of reports can be found in the literature regarding its hot deformation characteristics under different conditions, with different initial microstructures.

A study regarding the hot-working response of 718Plus was published previously by the authors.<sup>2</sup> This study is focused on a precipitate-free initial microstructure with relatively large grains (herein, this initial state is referred to as “baseline”). The focus of the current study, on the other hand, is on the amount of  $\gamma'$  in the initial microstructure and its effect on the deformation behavior. This may be particularly of interest to design the last forging stages in industrial processing of the alloy. The previously reported baseline behavior and model parameters may be useful to create contrast and understand some particularities found in the current study.

Unlike alloy 718, the main strengthening phase of 718Plus is  $\gamma'$  Nickel aluminite ( $\text{Ni}_3[\text{AlNbTi}]$ ), L12, cubic instead of  $\gamma''$  ( $\text{Ni}_3\text{Nb}$ , D022, tetragonal). The aforementioned increase of the temperature capability is believed to originate from the stability advantage of  $\gamma'$  over  $\gamma''$ .<sup>3–6</sup>

The importance of the  $\delta/\eta$  phase, in terms of grain size control and stress rupture properties, is well known in alloy 718. Because the appearance and precipitation behavior of the grain boundary (GB) precipitates in 718Plus were found to be similar to that of  $\delta$  phase of 718, they were initially identified as  $\delta$  phase ( $\text{Ni}_3\text{Nb}$ , D0a, orthorhombic) as well.<sup>7–9</sup> However, it was later studied in depth by Pickering et al.<sup>10</sup> and reported that the GB precipitates mainly consist of layers of  $\eta$  phase ( $\text{Ni}_6\text{Nb}[\text{Al Ti}]$ , D024, hexagonal) and accompanied with fine  $\delta$  layers. This nomenclature is not important given the focus of the current work.

A Time Temperature Transformation (TTT) diagram of the alloy was previously presented by Xie et al.<sup>11</sup> A partially agreeing precipitation–time–temperature (PTT) diagram was published by the current author.<sup>2</sup> According to these,  $\gamma'$  precipitation nose is in the range of 900°C–925°C. Around 950°C, the transformation line can be accepted as horizontally asymptotic. According to the same TTT, supplied by Xie et al.,<sup>11</sup> the  $\delta$  solvus temperature is given as 1,060°C.

Hot working consists of forming operations conducted at temperatures higher than  $0.5T_m$ . During these operations, different metallurgical processes may take place concurrently and interact with each other. These processes include work hardening (WH), dynamic recovery (DRV), and dynamic recrystallization (DRX) and may be accompanied by phase transformations, etc. Thus, comprehension of the underlying mechanisms and their relationship with forming parameters is essential to design better processes and to optimize the service performance and production costs.

Starting from the late 60s and early 70s, many studies focusing on the deformation behavior of metals at high homologous temperatures were reported. A review of the studies focusing on mathematical modeling flow curves showing single-peak DRX behavior was published by Ebrahimi and Shafiei.<sup>12</sup>

Apart from this, an ample amount of studies can be found in the literature regarding the hot deformation behavior of microalloyed steels.<sup>13–22</sup> Although the precipitating phases are different in nature in nickel-based

**TABLE 1**

Chemical compositions in wt. percent of IN718, 718Plus

Alloy	Ni	Cr	Mo	W	Co	Fe	Nb	Ti	Al
718	Bal	18.1	2.9	...	...	18	5.4	1	0.45
718Plus	Bal	18	2.8	1	9	10	5.4	0.7	1.45

superalloys, these studies are particularly interesting from the perspective of current study because both 718Plus and microalloyed steels (especially with niobium) show similar precipitation–hot deformation behavior.

Although one of the most comprehensive studies regarding the effect of precipitation in microalloyed steels was published by Jonas and Weiss<sup>15</sup> in the late 70s, recently, some models were constructed in order to include the effects of second-phase particles. Bäcke et al.<sup>23</sup> put effort on modeling precipitation and its effects on DRX in niobium microalloyed steels. Tancret, Galindo-Nava, and Díaz-del-Castillo<sup>24</sup> modeled the effect of  $\gamma'$  influence on the retardation of DRX through a net driving force analysis.

This work uses the well-known Estrin–Mecking–Bergström<sup>25,26</sup> approach to define the dislocation density as a function of dislocation generation and annihilation/remobilization. In order to model the effect of second-phase particles, a third term is added into the dislocation density balance equation relating the precipitate radius and volume fraction directly to the dislocation density by damping the recovery term.

## Experimental Procedure

Cylindrical compression specimens with 4-, 5-, and 7.5-mm diameters were machined from a 718Plus billet with initial grain size of 62  $\mu\text{m}$ . The height to diameter ratio was 1.5 for the specimens with 7.5-mm diameter, whereas for the rest this value was 2. Baehr 805 A/D deformation dilatometer and Instron 4507 (fitted with molybdenum punches) were employed to conduct the tests.

Two sets of compression tests were performed. Set 1 consisted of 4 different temperature and strain rates, namely, 900°C, 950°C, 1,000°C, and 1,050°C, at strain rates of 0.001, 0.01, 0.1, and 1  $\text{s}^{-1}$ . Final strain was varied between 0.5 and 0.65 because of the intrinsic limitations of compression testing.

Tests of Set 2 were conducted at 920°C and 940°C with strain rate of 0.01  $\text{s}^{-1}$  on the specimens held at 850°C for a different amounts of time, similar to the approach given in.<sup>15</sup> Deformation was terminated at approximately 0.4 strain in order to stay below the maximum force capability of the equipment. Some specimens were quenched slightly before the peak stress in order to preserve the structure before the DRX initiation.

For the Set 1, the cycle consisted of 3 steps. Firstly, the specimens were subject to solutionizing for 1 h at 1,050°C and water quenched. The average grain size after this solutionizing treatment was measured to be 73  $\mu\text{m}$ . Secondly, a 10-min-long extra solution treatment was applied to avoid any precipitating particles prior to the deformation. This extra solution treatment was followed by cooling down to the deformation temperature (at 1.5°C/s) for compression testing. Testing was started after allowing approximately 3 min for homogenization.

For the Set 2, specimens solutionized at the same temperature (1,050°C) for 1 h, followed by water quench. Then specimens were aged at 850°C (for different amounts of time), followed by water quench. Finally, specimens were heated directly to the deformation temperature and compressed after allowing 3 min for homogenization. Tests were interrupted at around 90 $\pm$ 3 % of the peak stress.

The selection of the deformation temperatures in Set 2 were based on TTT diagram of 718Plus.<sup>2,11,27</sup> Because the nose of the  $\gamma'$  transformation is around 920°C, this is selected as one condition. Furthermore, because the transformation line for  $\gamma'$  on the TTT diagram becomes asymptotic at 940°C, this is picked as the second condition.

Because the aging temperature (850°C) and strain rate during deformation (0.01 $^{-1}$ ) are the same for all specimens in Set 2, in the rest of the text these specimens will be referred to with their deformation temperature and prior aging time, e.g., a specimen deformed at 920°C after 120 min of aging is named Specimen 920°C – 120'.

During the tests, boron nitride powder and tantalum foils were used to reduce the specimen–punch friction, and after the compression tests, the specimens are quenched with argon purging with a rate of 7.5°C/s.

For transmission electron microscopy (TEM) analysis, the specimens were thinned with silicon carbide papers down to 20–30  $\mu\text{m}$  and electropolished with 5 % perchloric acid in ethanol at 32 V at  $-10^\circ\text{C}$ . Some specimens were extracted through Focused Ion Beam (FIB); however, the final quality was observed to be inferior to the electropolished specimens. TEM examinations were performed with a Jeol ARM 200F operated at 200-kV acceleration voltage. All specimens were plasma cleaned in order to remove surface oxides and impurities before TEM.

## Modeling Approach

### WH OF INITIAL MATERIAL

In the formalism of WH, the following relationship given in equation (1), known as Taylor's Equation, is accepted to well form the bridge between the flow stress ( $\sigma$ ) and dislocation density ( $\rho$ ).

$$\sigma = \sigma_i + \mu \alpha b \sqrt{\rho} \quad (1)$$

In this relationship,  $m$  is orientation/texture factor,  $\alpha$  is a proportionality factor,  $\mu$  is the shear modulus, and  $b$  is the magnitude of the Burgers vector.

$\sigma_i$  is usually referred to as friction stress. The definition of this term is somewhat ambiguous<sup>28</sup> even if some authors relate it to the contribution of grain size hardening, precipitation hardening, solution hardening, etc. Within this study, as the model results of the aged specimens will be compared with the reference (solutionized) condition; the only contribution is assumed to be originating from precipitation hardening. Thus, it will be named  $\sigma_p$ .

To be fully described, the second term in equation (1) necessitates a model describing the evolution of the dislocation density fed in. To this end, a model initially proposed by Estrin and Mecking and Bergström is adapted and implemented in this study. According to this, the dislocation evolution in the time domain through the equation (2):

$$\frac{d\rho}{dt} = U \frac{d\epsilon}{dt} - \Omega \rho \left[ 1 - \frac{g}{\sqrt{\rho}} \right] \frac{d\epsilon}{dt} \quad (2)$$

where  $t$  is time and  $\epsilon$  is the strain.  $U$  is the athermal WH in the form of ( $= \frac{m}{bL}$ ).  $L$  is the mean free path of dislocations, which they can travel until immobilized by a barrier (pile up), obstacle (second-phase/precipitate), or both.

The second term in the equation (2) represents DRV.  $\Omega$  is a strain-independent material constant representing the dislocation remobilization in the absence of precipitation. Note the damping term attached to this term, which represents the effect due to the precipitation, which was first proposed by Engberg and Lissel,<sup>16</sup> Bäcke,<sup>18</sup> and Lissel, Engberg, Borggren<sup>23</sup> to limit the softening due to climb only. Here,  $g$  can be expanded as  $g = C(f_{prec}/r_{prec})$ , where  $f_{prec}$  and  $r_{prec}$  represent volume fraction and radius of the second-phase particles, and  $C$  is a parameter, similar to the dislocation density factor introduced by Dutta, Palmiere, and Sellars<sup>20</sup> Here, it is important to mention that in this work, only up to moderate volume fractions of  $\gamma'$  with spherical morphology are considered, agreeing with the TEM observations.

The mean free path of dislocations is calculated based on the subcell diameter and precipitation. They were assumed to additively contribute to the immobilization of the dislocations, which is given in equation (3).

$$\frac{1}{L} = \frac{\sqrt{\rho}}{K_{cell}} + \frac{K_{prec}}{L_{prec}} \quad (3)$$

where  $K_{cell}$  and  $K_{prec}$  are parameters that define the immobilization effectiveness.<sup>29</sup> The original model<sup>30</sup> assumes an evolution from  $L_{start}$  to  $L_{end}$ . In the current case, this is assumed to be constant, which is fair, considering the original treatment was on ferrite. Moreover, for the solutionized material, it is assumed that the cell spacing is smaller than precipitate spacing. Therefore, the hardening contribution from the precipitates is ignored in this case. The exact value of  $L_{prec}$  is calculated based on a statistical representation<sup>31</sup> of randomly distributed spherical particles whose reduced form is shown in equation (4).

$$L_{prec} = \sqrt{\frac{\log(3)}{2\pi Nr} + \frac{8}{3}r^2} - \frac{8}{3}r^2 \quad (4)$$

where  $N$  and  $r$  are the number density and particle radius, respectively.

**TABLE 2**  
 $\gamma'$  volume fraction and radius of deformed alloy

Temperature	Volume Fraction	Radius
<940°C	0.091	3.1843 $r^{1/3}$
>940°C	0.091	2.9143 $r^{1/3}$

Furthermore, in order to define both equations (4) and (2), one needs a description of the volume fraction and particle size of the precipitates. These can be obtained through numerical models for precipitation or based on experimental data. The radius data presented by Radis et al.<sup>32</sup> and Zickler et al.<sup>33</sup> considering static precipitation are found to underestimate the second particle radius when compared with the current findings below 940°C. Thus, the models they presented are calibrated according to  $\gamma'$  radius observed in the deformed specimens in this study. Accordingly, the volume fraction and precipitate radius values are summarized on Table 2.

MATLAB 2017a was used for the numerical treatment and estimation based on the experimental hot flow curves. The temperature dependence of the magnitude of Burgers vector ( $b$ ) is ignored and taken as  $2.56 \times 10^{-10}$  m. The constants  $m$  and  $\alpha$  are assumed to be strain independent and taken as 3.1 (close to the 12-slip system value, 3) and 0.15, respectively. Initial dislocation density,  $\rho_0$ , is taken as  $1 \times 10^{12}$  m/m<sup>3</sup>. The values for hardening recovery rate for Set 2 are calculated based on the previously reported Zener–Hollomon ( $Z$ ) dependency for Set 1.<sup>2</sup> The temperature dependency of the shear modulus is considered through equation (5).<sup>34</sup>

$$\mu(T) = \mu_0 \exp\left(1 - \frac{T - 300}{T_m}\right) \quad (5)$$

### PRECIPITATION STRESS AND ITS COMPONENTS

During (hot) deformation, when a dislocation meets a precipitate, it can either loop around the particle or cut through it. The former is usually called the Orowan mechanism, and the latter is occasionally referred to as precipitation shearing. The stress contribution (the stress necessary to make a dislocation overcome all the obstacles on its way) of these mechanisms is given by equations (6) and (7), respectively.

$$\sigma_{Loop} = \frac{2.43\mu b_\gamma}{4\pi(L_p - 2r)} \beta \ln\left(\frac{L_p - 2r}{2b_\gamma}\right) \quad (6)$$

$$\sigma_{Cut} = \frac{m\mu b_{\gamma'}}{r\sqrt{\pi w_q}} k_c \sqrt{f} \left(\frac{2\gamma_{APB} w_r r}{\mu b_{\gamma'}^2}\right)^{3/2} \quad (7)$$

where  $\mu$  is the shear modulus,  $b$  is the magnitude of Burgers vector,  $L_p$  is the interparticle spacing,  $r$  is the precipitate radius, and  $\gamma_{APB}$  is the energy density of the planar antiphase boundary.  $w_r$  and  $w_q$  are constants.<sup>35</sup>  $\beta$  and  $k_c$  are calibration constants taken from the approach of Fisk et al.<sup>29</sup>

Although the activity of these mechanisms can be observed qualitatively through TEM observations, the contribution of each cannot be quantified. Because of this, the overall contribution is assumed to be a weighted average of the two, as given in equation (8).

$$\sigma_{Total} = f_{Cut} \sigma_{Cut} + (1 - f_{Cut}) \sigma_{Loop} \quad (8)$$

where  $f_{Cut}$  is the volume fraction of precipitates passed by the shearing mechanism. A straightforward solution would be obtained through calculating the fraction of sheared (cut) precipitates by using a size distribution function and assuming a critical size for mechanism transition from cutting to looping. However, in the current case, an inverse approach is used, and  $f_{Cut}$  is reported as a function of aging time. Constants  $\beta$  and  $k_c$  are found based on the assumption that after 2 h of aging at 850°C the dominating mechanism is particle looping.

## Results and Discussion

The current text intends to report the two parallel investigations, i.e., the characterization and the modeling the deformation behavior from a perspective that prioritizes  $\gamma'$  precipitation. To this end, first, some highlights of the TEM/Scanning Transmission Electron Microscope (STEM) characterization of the undeformed, deformed, aged, and unaged specimens will be given, and later, the model results will be presented. Some of the results, especially those regarding the effect of  $\gamma'$  on the deformation behavior, play an important role in the selection of suitable models, the selection of plausible values of certain model parameters, or both. These are highlighted in the text when necessary.

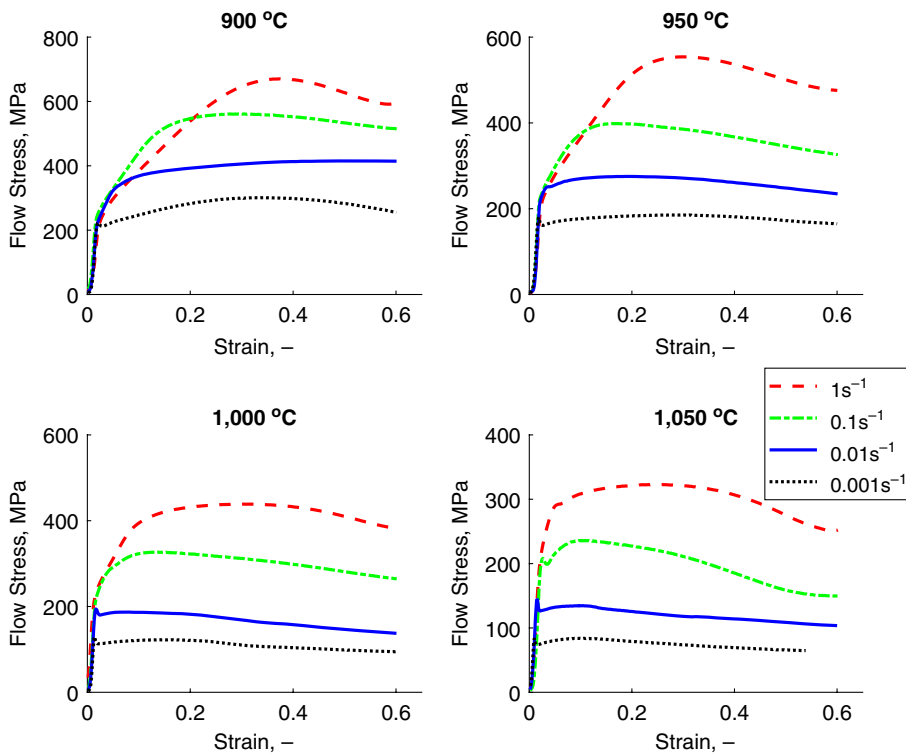
### HOT DEFORMATION BEHAVIOR OF UNAGED SPECIMENS

The flow curves of the tests belonging to Set 1 described in the “Experimental Procedure” are given in [figure 1](#). In general, flow curves show a classical single peak DRX behavior. No cyclic DRX behavior is observed. Because at higher temperatures, the stress to initiate the DRX is lower and precipitation is unfavorable, the nucleation of new strain-free grains is expected to be easier. Thus, this is an expected scenario to observe. Moreover, the DRX kinetics are expected to be higher at high temperatures because of the higher GB mobility. When these facts are considered, the obtained results within Set 1 can be considered as natural.

Moreover, it can be said that the strain curves at 900°C and 950°C generally show lower hardening slopes when compared with previously published data.<sup>36</sup> Unfortunately, these authors did not share the complete set of data, so it is not possible to make a better comparison.

The material constants defining the WH of the material and detailed discussion of the general hot flow behavior is presented elsewhere.<sup>2</sup> Previously apparent values of  $\Omega$  and  $U$  are given as a function of  $Z$ . This relationship can be defined through  $\Omega = K_{\Omega}Z^{m_{\Omega}}$  and  $(\alpha'b)^2U = K_UZ^{m_U}$ , where  $K_{\Omega}$  and  $m_{\Omega}$  were reported as

**FIG. 1** Flow curves of Set 1 obtained at 900°C, 950°C, 1,000°C, 1,050°C, and 0.001, 0.01, 0.1, and 1 s<sup>-1</sup> strain rates.



8,020,  $-0.1155$ ;  $K_U$  and  $m_U$  as  $5.083e-06$  and  $0.1069$ , respectively. These DRV rate parameters do not take into account the precipitation effects as they are apparent in nature.

### THE EFFECT OF GAMMA PRIME ON THE HOT DEFORMATION BEHAVIOR

As mentioned earlier, in this investigation, an attempt has been made to follow the effects of  $\gamma'$  particles on the high-temperature flow behavior. Tests within Set 2 were conducted on specimens solutionized at  $1,050^\circ\text{C}$  for 1 h followed by water quenching, then aging at  $850^\circ\text{C}$  different times, and finally, water quenching prior to the deformation. The resulting flow curves are presented in **figure 2** until 0.35–0.45 strain.

A few details can be noted immediately by observing the flow curves. Firstly, a convergence in the flow behavior with longer aging times observed after almost 2 h of aging. Secondly, some curves ( $920^\circ\text{C}-0'$ ,  $940^\circ\text{C}-0'$ , and  $940^\circ\text{C}-10'$ ) present a serration/double yield at the very initial stages of deformation. This is observed in some of the flow curves of Set 1 as well.

The effect of aging seems to manifest itself on the flow curve as if there was an increase of the Z. This is accompanied by the vanishing of the aforementioned serration/double yield and a slight change in the slope of the curves in the elastic section. The slope change and the “double yielding” behavior was also observed by Wen et al.,<sup>37</sup> who compared the WH behavior of a nickel-based superalloy in the solutionized and aged state. This might be related to the diffusion of the  $\gamma'$  forming elements and deformation speed; however, this is out of the scope of the current investigation.

In 1979, Jonas and Weiss<sup>15</sup> presented a report, stating that the consideration of yield strength to observe the effect of precipitation, to estimate the precipitation kinetics, or both, is not the optimum method because of its

**FIG. 2**

Hot flow response of different specimens aged at  $850^\circ\text{C}$  for different times. Upper image:  $920^\circ\text{C}$ ,  $0.01\text{ s}^{-1}$ ; lower image:  $940^\circ\text{C}$ ,  $0.01\text{ s}^{-1}$ .

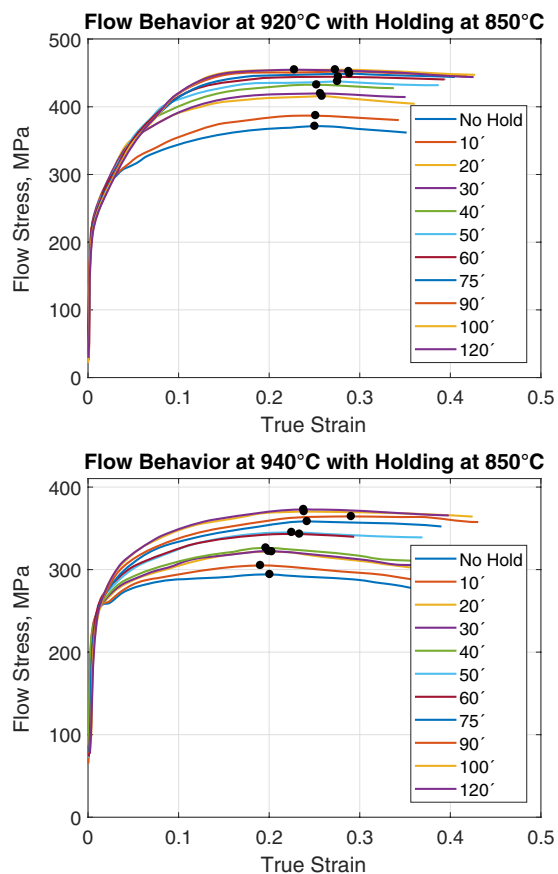
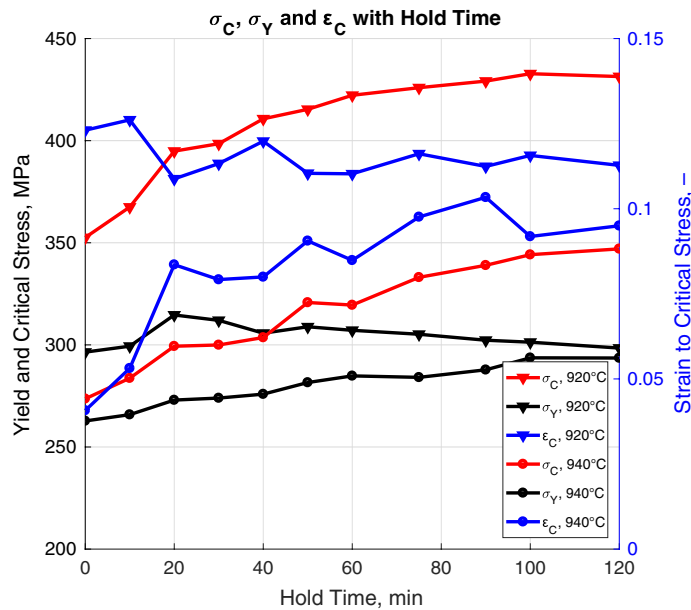


**FIG. 3**

Effect of aging on different characteristic points of the flow curve: strain needed for critical stress ( $\epsilon_C$ ), critical stress ( $\sigma_C$ ), and yield strength ( $\sigma_Y$ ) are plotted as a function of aging time.



insensitivity/oversensitivity. In the current case, yield strength against the aging time is presented; however, they are not used in any quantitative/numerical evaluation. Furthermore, these authors<sup>15</sup> found that strain to peak stress is a more reliable parameter to track the effects of precipitation. The evolution of critical stress, yield strength, and strain to critical stress is given in figure 3. The critical aforementioned analysis is found based on the formulation of Najafizadeh and Jonas.<sup>38</sup>

Conversely to the findings of Jonas and Weiss,<sup>15</sup> here, the strain to critical stress does not decrease to converge a value. The decrease of the critical strain in their case (earlier start of DRX) is explained by the lack of dynamic precipitation. When the specimen is held before deformation, as the static precipitation evolves, the matrix remains depleted of precipitate forming elements, thus reducing the potential of dynamic precipitation.

In the current investigation, the opposite is observed, i.e., longer aging times result in delays in the critical strain. Although this is not the core point of the current work, this might be a result of a combination of few facts. First, the precipitating phases in niobium-microalloyed steels (Nb(C,N)) and superalloys are different in nature when their relationship with the matrix is considered. The coherency/semicoherency for the precipitates in microalloyed steels is usually lost for precipitate sizes larger than 10 nm.<sup>39</sup> Thus, with aging, precipitates formed prior to the deformation might not contribute the retardation of DRX as efficiently as the dynamically precipitating ones. Secondly, probably as Srinivasan, Lawless, and Ott<sup>27</sup> and Andersson et al.<sup>40</sup> reported, after solutionizing at relatively higher temperatures (above 1,012°C) the subsequent  $\delta/\eta$  precipitation becomes very sluggish (due to the growth of the original grains). This makes the microstructure starve the preferential DRX nucleation sites. Because of the absence of GB precipitates, the effect of  $\gamma'$  on DRX onset potentially become more pronounced. However, further investigation would be necessary to clarify this.

### MODELING THE OBSERVED BEHAVIOR

Table 3 shows the model parameters. A comparison of measured and computed stress–strain curves for 0, 30, and 120 min of aging are shown in figure 4. Here, the model is calibrated only for no or little aging times when compared with industrial routines (up to 8 or 16 h of aging). The resultant mean error over the strain interval averaged through all conditions is 11.37 MPa, which is acceptable considering the modifications made to the base models. Although the deformation is assumed to be homogeneous, to account for the effect of precipitation, it was

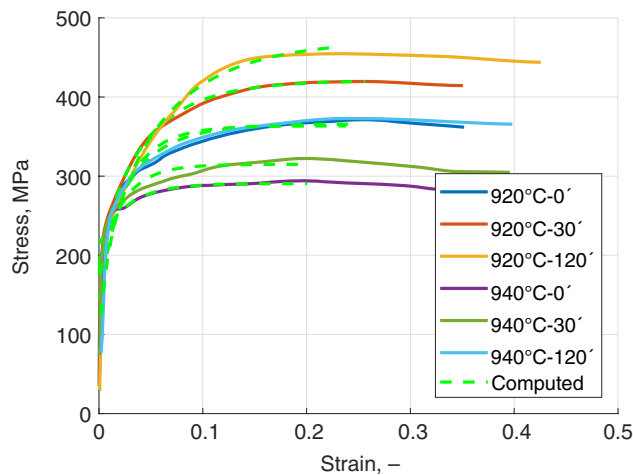
**TABLE 3**

Model parameters and results

Parameter	920°C-0.01 s <sup>-1</sup>	940°C-0.01 s <sup>-1</sup>	Unit
$\alpha$	0.15	0.15	...
$b$	$2.56 \times 10^{-10}$	$2.56 \times 10^{-10}$	m
$m$	3.1	3.1	...
C (when constant)	0.11	0.08	...
$\Omega$	33.82	37.35	...
$U$	$8.020 \times 10^{-4}$	$7.318 \times 10^{-4}$	...
$\rho_0$	$1 \times 10^{12}$	$1 \times 10^{12}$	m/m <sup>3</sup>
$K_{prec}$ (no hold)	0	0	...
$\mu$	equation (5)	equation (5)	GPa
$w_q$	0.75	0.75	...
$w_r$	0.82	0.82	...
$\gamma_{APB}$	0.111	0.111	J/m <sup>2</sup>
$\beta$	0.29	0.31	...
$k_c$	0.08	0.09	...

**FIG. 4**

Measured and calculated flow curves of solutionized and aged (30 and 120 min) specimens. Dashed lines represent calculated values.

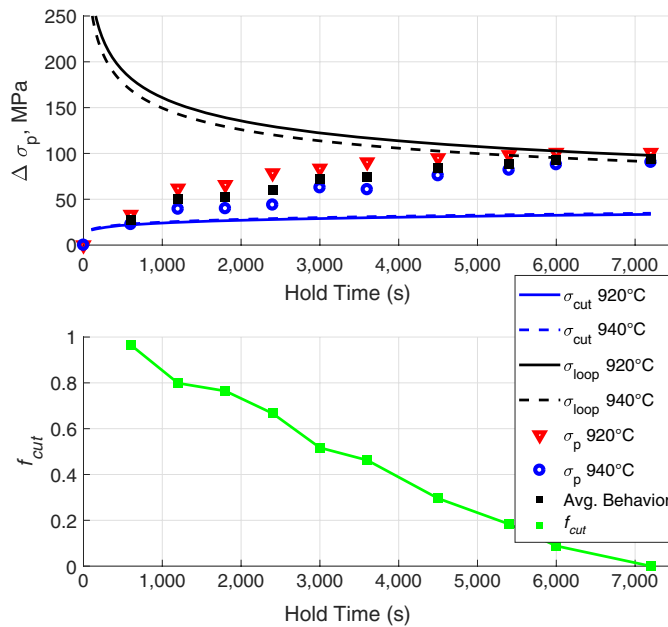


necessary to introduce more model parameters. Although the number of parameters is quite high relative to the simplistic models, the model is still applicable. To simplify the treatment, the factor  $C$  can be accepted as a constant when the deformation duration is short relative to the precipitation kinetics. Plausible values for this factor are given in [Table 3](#).

To evaluate how  $f_{cut}$  evolves with aging time, the contribution of second-phase particles is considered through equations (6) and (7) based on the change in  $\sigma_p$  of equation (1). This is summarized in [figure 5](#). When calculating the contribution of yield stress at room temperature, the critical radius/aging time can be found by equating the equations (6) and (7). When this is applied to the current case, one finds the critical aging time to be 4,000 s (taking  $\beta = 1$  and  $k_c = 1$ ). However, this would not correlate with the findings of the TEM study. After calibrating equations (6) and (7) and using the equation (8), one finds that at about 1,200–1,800 s of aging, the Orowan mechanism is active. The critical radius for similar alloys is reported to be around 12 nm,<sup>41,42</sup> which is in line with the current findings. However, the very same alloy was previously studied by Zickler et al.<sup>33</sup> for room-temperature yield strength predictions, and they reported particle shearing as the main mechanism governing the

**FIG. 5**

Contributions of different particle hardening mechanisms given together with the calculated increase in  $\sigma_p$  of equation (1).



precipitation contribution. This raises the question whether high-temperature deformation favors the Orowan mechanism or not. Furthermore, the validity of the equations (6) and (7) to evaluate the particle strengthening at high temperatures can be questioned. From physics-based modeling, there should not be any calibration constants associated with contributions independent of strain.

## TEM and STEM Observations

**Figure 6** shows a series of TEM and STEM images of an undeformed specimen aged at 850°C for 30 minutes. A bright-field (BF) TEM image giving an overview of the microstructure is given in **figure 6A**.  $\gamma'$  precipitates accompanied by a sparse amount of twins are observed together with stacking faults (SF).

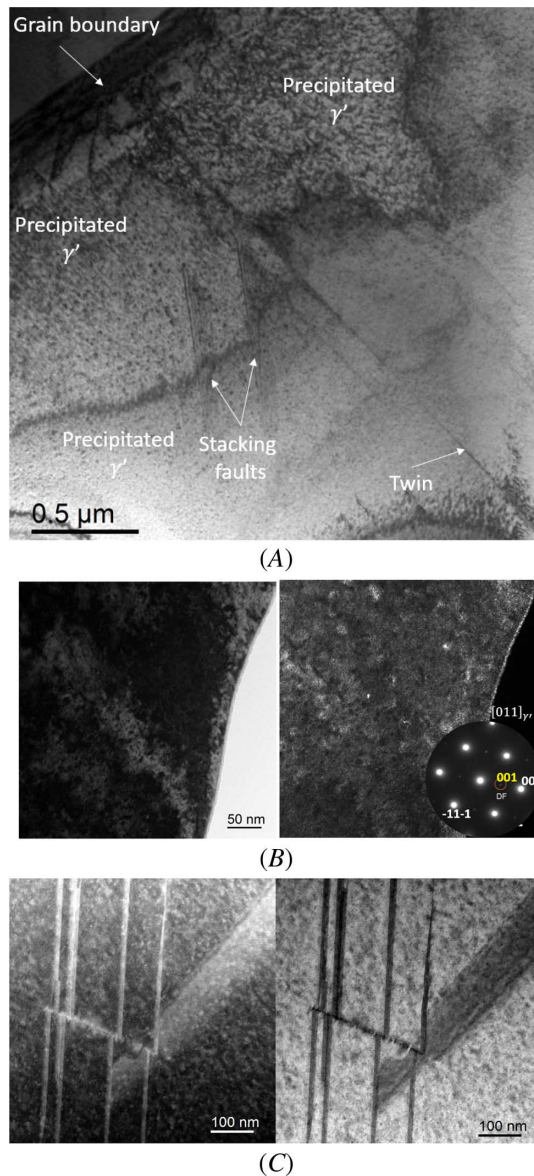
In general, all observed specimens point out two different families of  $\gamma'$ , one consisting of fine (<10 nm) densely distributed population, and the other consisting of larger, spherical (faceted) and homogeneously distributed precipitates, different in size depending on the aging time. The appearance of two different  $\gamma'$  populations is found to be more pronounced for specimens in Set 2 (deformed after preaging). This is in line with the findings of Whitmore et al.,<sup>43</sup> in which the authors analyzed single- and double-aged 718Plus and reported both treatment routines result in a very fine (1–2 nm)  $\gamma'$  as a secondary precipitate population. The smaller  $\gamma'$  size for their case is expected as the aging temperature was below 790°C for Whitmore et al.<sup>43</sup>

These  $\gamma'$  particles can be observed both in **figure 6B** and **6C**. The former pair represents BF TEM images and corresponding dark-field (DF) TEM image recorded using (100) superlattice reflection. The latter is BF and high-angle annular DF (HAADF) STEM images recorded in a region where  $\gamma'$  is observed accompanied with planar defects, which might be twins, SF, or antiphase boundary (APB).

As mentioned in the experimental section, Set 2 specimens were deformed up to near-critical strain after different aging treatments. BF and corresponding DF TEM images using (001) superlattice reflection from 2 different regions of the 920°C-20' (for terminology selection, refer back to "Experimental Procedure") specimen are shown in **figure 7**.

**FIG. 6**

TEM images after solutionizing at 1,050°C followed by 30-min aging at 850°C: (A) low-magnification image giving an overview of the microstructure, (B) BF (left) and corresponding DF (right) images recorded along  $[011]_{\gamma'}$ // $[011]_{\gamma'}$  zone axis. (C) STEM images: BF (right) and corresponding HAADF (left).



These images are recorded on the same grain. Whereas [figure 7A](#) shows fine and densely distributed  $\gamma'$ , [figure 7B](#) shows spherical particles having average size of 39.8 nm. Even though most of the observed regions have the latter form of spherical  $\gamma'$  (see also [fig. 8](#) for Energy Dispersive X-Ray Spectroscopy [EDX] maps), it is thought-provoking that there are regions within the same grain where a finer and denser  $\gamma'$  population is observed. This inhomogeneity can be either associated with that of the deformation or due to a zone depleted of  $\gamma'$  forming elements. As highlighted by Miltzer, Sun, and Jonas,<sup>44</sup> vacancy concentration levels during hot deformation might attain as much as 40 times that of equilibrium concentrations for a given temperature. Thus, any inhomogeneity in the dislocation density within a grain might cause local variations in precipitation characteristics. For the calculations performed within this study, only the spherical  $\gamma'$  population is considered to have an effect on the dislocation path.

**FIG. 7** TEM BF (A) and corresponding DF (B) images of aged (850°C for 20 min) and deformed (920°C, 0.01 s<sup>-1</sup>) specimen. Both DF images were recorded using (001) weak superlattice reflection.

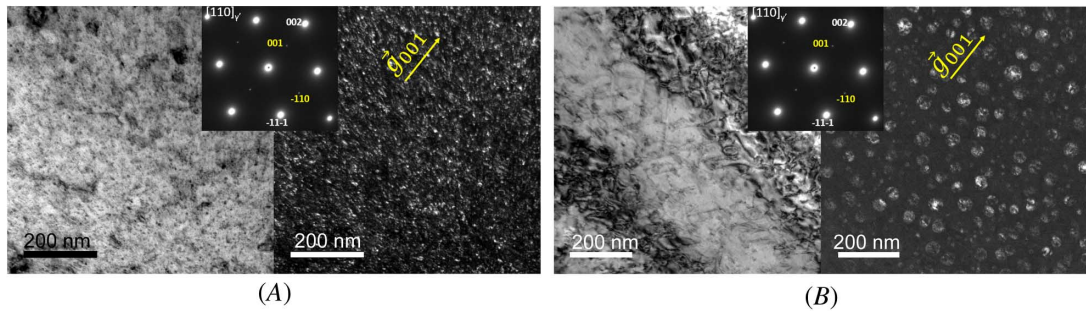


**FIG. 8**

EDX maps of aged and deformed: (A) 920°C-20' and (B) 940°C-30'.

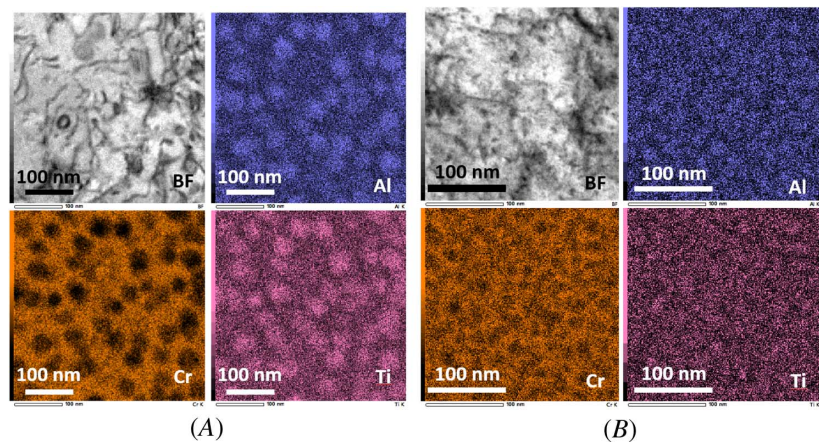


**Figure 8** gives the elemental maps (EDX maps) recorded on specimens 920°C-20' (**fig. 8A**) and 940°C-30' (**fig. 8B**).  $\gamma'$  can be associated with the chromium-depleted and aluminum/titanium-rich zones. Only chromium, aluminum, and titanium elements are presented to highlight the contrast. As mentioned in the experimental section, 920°C and 940°C are the temperatures at which the nose and asymptote of  $\gamma$ - $\gamma'$  transformation line are located on the TTT diagram, respectively. Based on **figure 8B**, the  $\gamma'$  obtained during preaging treatment is preserved to a large extent during deformation at 940°C. In contrast,  $\gamma'$  observed in 920°C-20' is very well defined, leading one to consider the contribution of deformation to  $\gamma'$  growth when the deformation takes place in the precipitation window (below 940°C). The effect of deformation on the nucleation of  $\gamma'$  might be considered based on **figure 7B**; however, further examination would be necessary. Furthermore, considering the overall volume fraction of  $\gamma'$  before deformation, forced nucleation of  $\gamma'$  is of low probability.

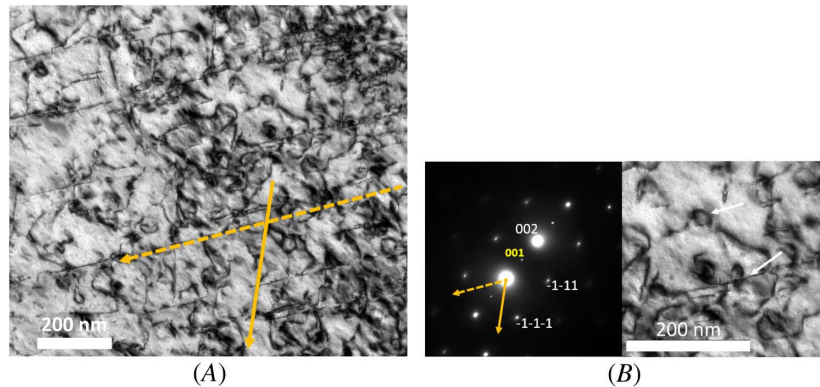
#### OBSERVATIONS ON THE AGED AND DEFORMED SPECIMENS

One of the objectives of TEM characterization in this study is to understand which dislocation-particle interaction mechanism(s) is active. This is particularly important when evaluating the effect of aging on the integrated/overall mechanical response of the alloy.

To this end, the weak-beam technique has been used. Based on the observations, dislocation bowing and looping can be clearly observed, and cutting cannot be ruled out. **Figure 9** shows a set of BF images

**FIG. 9**

(A) BF TEM image with approximate zone axis [011]. (B) A portion of the image shown on (A) highlighting interaction modes.



obtained from specimen 920°C-20'. **Figure 9A** gives an overview, and the upper arrow on the image given in **figure 9B** shows a dislocation bowing around a precipitate, and the lower one shows a dislocation cutting a precipitate (the dashed line given is  $[1\bar{1}\bar{2}]$ ). This result is interesting because Zickler et al.<sup>33</sup> reported the experimental and predicted room temperature yield strength of 718Plus for aging times up to 200 min at 825°C. These authors highlight that the predictions based on the Orowan mechanism overestimate the experimental values more than 1.5 times for all aging times. In their work, they conclude that the Orowan mechanism becomes active only after 50 min of aging time at 825°C. Compared with this, in the current case while 20-min preaging time is rather short, traces of the Orowan mechanism can be clearly observed.

Furthermore, **figure 10** shows BF and weak-beam DF images of 920°C-20' specimen. In the DF images some characteristic fringes are clearly visible. There may be many reasons for the formation of these fringes. They could be attributed to moiré, to SF bounded by partial dissociations, Shockley dislocations resulting from perfect dislocation dissociation, etc. The fringes could appear during the shearing of precipitates by the matrix dislocations, recalling the Condat-Décamps mechanism.<sup>45,46</sup>

It is well established<sup>47</sup> that the SF alternates parallel bright and dark fringes, the outer of which does not have the same contrast; when the image is recorded in DF mode, the image is called asymmetric. The insert in DF image of **figure 10B** point out a series of alternate bright and dark fringes, and the outer fringes have the same bright contrast. Based on this behavior, the SF are excluded; thus, we are left with the moiré fringes. A slight disorientation of less than 1° was detected. This configuration strongly argues in favor of mixed moiré fringes (translation + rotation) obtained by the superposition of the matrix and precipitates. The departure to the exact cube-cube relationship should be attributed to stress relaxation during the shearing of the precipitates by the matrix dislocations.

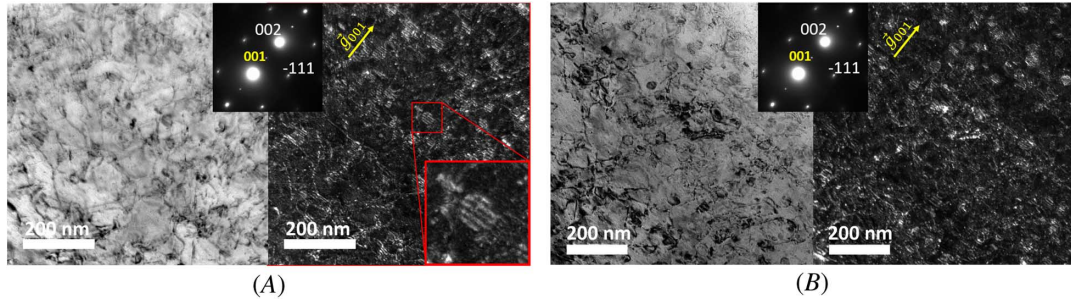
**TABLE 4**

Determination of  $H$ , the intersection point group, the elements of which are common to the point groups of  $\gamma$  and  $\gamma'$  phases

Orientation Relationship	Superimposed Symmetry Elements	Shared Symmetry Elements	$H = G' \cap G'$ with $n = \frac{m}{h}$
$(002)_{\gamma} // (001)_{\gamma'}$	$\frac{4}{m} // \frac{4}{m}$	$\frac{4}{m}$	
$(1\bar{1}1)_{\gamma} // (1\bar{1}1)_{\gamma'}$	$\bar{3} // \bar{3}$	$\bar{3}$	$\frac{4}{m} \bar{3} \frac{2}{m}$
$(220)_{\gamma} // (1\bar{1}0)_{\gamma'}$	$\frac{2}{m} // \frac{2}{m}$	$\frac{2}{m}$	with $n = 48 / 48 = 1$

Note:  $n$  is the number of variants;  $m$ ,  $p$ , and  $h$  are the orders of the point groups of matrix, precipitate, and intersection group, respectively.

**FIG. 10** BF (A) and weak-beam DF (B) TEM images of 920°C-20' specimen after deformation. Weak-beam image (g-3 g) g = 001 recorded along zone axis close to [011].



Additionally, a BF TEM image of 940°C-0' specimen (specimen with no prior aging) is shown in [figure 11](#), presenting abundant  $a/2\langle 110 \rangle$  matrix dislocations with evidence of cross slip (note the rigged appearance of the dislocations). This is an interesting detail as no significant precipitation is observed in this specimen. Under normal circumstances, an increase in cross-slip probability (and thus an increase in recovery parameter  $\Omega$ ) would be expected in an aged alloy relative to the solutionized one. Based on this in the current case,  $\Omega$  is assumed to be independent of precipitation.

#### MORPHOLOGY OF $\gamma'$ AND ITS RELATIONSHIP WITH $\gamma$ MATRIX

The  $\gamma'$  precipitates adopt an usual cube-on-cube orientation relationship with the matrix where it develops as derived from the analyzed selected area electron diffraction (SAED) patterns. This relationship can be expressed by the parallelism between the corresponding planes and can be expressed as follows:

$$(002)_{\gamma'} // (001)_{\gamma'} \quad (1\bar{1}1)_{\gamma'} // (1\bar{1}1)_{\gamma'} \quad (2\bar{2}0)_{\gamma'} // (1\bar{1}0)_{\gamma'}$$

Trace analysis indicates that the  $\gamma'$  phase develops only one variant in each matrix grain (see [fig. 7B](#) as well). [Figure 12](#) shows a high-resolution image of a 30-min aged specimen at 850°C after solutionizing at 1,050°C. The inset is the corresponding fast fourier transform (FFT) recorded along  $[011]_{\gamma'} // [011]_{\gamma'}$ .

#### SYMMETRY ANALYSIS

It is well established, through the group theory, that the morphology of phases, taking place in any medium (solid, liquid, or gas) is of great importance in materials science. Understanding of both the equilibrium shape and the habit plane adopted by these phases in their medium is widely investigated.<sup>48-55</sup> We will apply this group theory, based on the symmetry analysis, to explain the shape developed by the  $\gamma'$  phase and its variant number.

When the point symmetry groups of  $\gamma$  matrix and  $\gamma'$  precipitates are considered ( $G_{\gamma}$  and  $G_{\gamma'}$ ), if the precipitating phase adopts an orientation relationship with the matrix, the intersection point group ( $H$ ) will

**FIG. 11**

BF TEM image of 940°C-0' specimen. (a/2) $\langle 110 \rangle$  type of matrix dislocations.

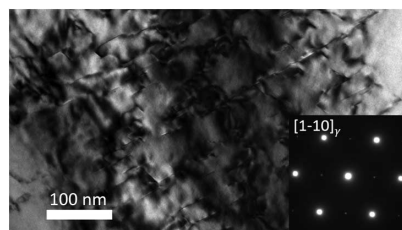
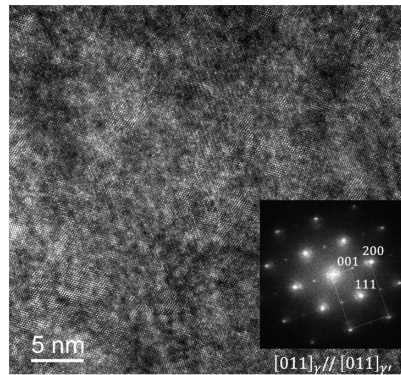


**FIG. 12**

High-resolution TEM image and its corresponding FFT recorded along  $[011]_{\gamma} // [011]_{\gamma'}$  zone axis.



be represented by their common symmetry elements. Usually denoted as  $H = G' \cap G''$ .  $H$ , the subgroup of the matrix and of the precipitate point groups the morphology of the precipitate together with the variant number  $n$  of the subgroupings. The latter helps to assess the number of variant(s) taking place in the matrix and satisfying the orientation relationship adopted between the matrix and the precipitate. The variant number  $n$  is the ratio  $n = m/h$ , where  $m$  and  $h$  are the orders  $G'$  and  $H$ , respectively. This analysis is summarized in [Table 4](#). Accordingly, the point group of the matrix ( $G'$ ) is  $\frac{4}{m}\bar{3}\frac{2}{m}$ , which is the same as that of the  $\gamma'$  ( $G''$ ). Obeying the orientation relationship, the superimposition of the symmetry elements of the two  $\frac{4}{m}\bar{3}\frac{2}{m}$  point groups preserves all symmetry elements, leading to  $H = \frac{4}{m}\bar{3}\frac{2}{m}$ .

The fact that both  $G'$  and  $G''$  have the order of 48 leads to the variant number  $n = 1$ , indicating that there is only one variant of the  $\gamma'$  formation in  $\gamma$  matrix. This is in line with the observations, i.e., faceted spherical and cubic  $\gamma'$  in  $\gamma$  depending on the volume fraction. In the case of 718Plus, we observe mostly fine or faceted spherical precipitates, see [figure 7B](#) and EDX maps in [figure 8A](#).

## Conclusions

The hot flow behavior or solutionized and preaged 718Plus is investigated. Two different sets of tests are performed: Set 1, which consists of solutionized specimens being deformed at 16 different conditions (4 strain rate  $\times$  4 temperature) and Set 2, which consists of solutionized and preaged specimens being deformed at 2 different conditions (1 strain rate  $\times$  2 temperature). Up to 2 h of aging times are investigated, which might be of interest to design the final passes of industrial forging operations.

A homogeneous WH model based on the long-standing dislocation density theory is proposed, which includes the effect of precipitation as a damping factor of recovery rate. The evolution of precipitate volume fraction and radius is deduced based on the experimental findings reported in the literature and is calibrated according to the TEM observations. The proposed model is fitted to the experimental stress–strain curves up to the critical stress. The flow–stress contributions of different dislocation precipitation interaction mechanisms are evaluated, and it is found that the Orowan mechanism is activated around 1,200 s aging time, after which it quickly starts to dominate.

A symmetry analysis of  $\gamma - \gamma'$  is conducted, and the variant number of  $\gamma'$  phase is reported as 1, meaning only faceted spherical or cubic  $\gamma'$  is possible. Within this study, only very fine (<10 nm) or larger spherical  $\gamma'$  (size depends on aging time) is observed. An alteration in the precipitation kinetics compared with the previously reported static kinetics is observed; however, it is left out of the scope of the current study. Based on the TEM observations, after 1,000 s of aging time; bowing, looping, and cutting mechanisms are observed to be coactive.

## ACKNOWLEDGMENTS

The authors greatly acknowledge the European Union funding through Doctoral Programme in Advanced Materials Science and Engineering (DocMASE) Erasmus-Mundus program.

## References

1. E. A. Ott, J. Groh, and H. Sizek, "Metals Affordability Initiative: Application of Allvac Alloy 718Plus™ for Aircraft Engine Static Structural Components," in *Superalloys 718, 625, and Derivatives 2005* (Pittsburgh, PA: The Minerals, Metals, and Materials Society, 2005), 35–45.
2. U. Ozturk, J. M. Cabrera, and J. Calvo, "High-Temperature Deformation of Inconel 718Plus™," *Journal of Engineering for Gas Turbines and Power* 139, no. 3 (2017): 032101. <https://doi.org/10.1115/1.4034539>
3. X. Xie, G. Wang, J. Dong, C. Xu, W.-D. Cao, and R. Kennedy, "Structure Stability Study on a Newly Developed Nickel-Base Superalloy—Allvac® 718Plus™," in *Superalloys 718, 625, 706 and Derivatives* (Pittsburgh, PA: The Minerals, Metals, and Materials Society, 2005), 179–191.
4. R. Cozar and A. Pineau, "Morphology of  $\gamma'$  and  $\gamma''$  Precipitates and Thermal Stability of Inconel 718 Type Alloys," *Metallurgical Transactions* 4, no. 1 (January 1973): 47–59. <https://doi.org/10.1007/BF02649604>
5. L. Viskari and K. Stiller, "Atom Probe Tomography of Ni-Base Superalloys Allvac 718Plus and Alloy 718," *Ultramicroscopy* 111, no. 6 (May 2011): 652–658. <https://doi.org/10.1016/j.ultramic.2011.01.015>
6. A. Casanova, N. Martín-Piris, M. Hardy, and C. Rae, "Evolution of Secondary Phases in Alloy ATI 718® during Processing," *MATEC Web of Conferences* 14 (2014): 09003. <https://doi.org/10.1051/mateconf/20141409003>
7. W.-D. Cao, "Solidification and Solid State Phase Transformation of Allvac® 718Plus™ Alloy," in *Superalloys 718, 625, 706 and Derivatives* (Pittsburgh, PA: The Minerals, Metals, and Materials Society, 2005), 165–177.
8. W.-D. Cao and R. Kennedy, "Role of Chemistry in 718-Type Alloys—Allvac® 718Plus™ Alloy Development," in *Superalloys 2004* (Pittsburgh, PA: The Minerals, Metals, and Materials Society, 2004), 91–99.
9. C. Stotter, C. Sommitsch, J. Wagner, H. Leitner, I. Letofsky-Papst, G. A. Zickler, W. Prantl, and M. Stockinger, "Characterization of  $\delta$ -Phase in Superalloy Allvac 718Plus™," *International Journal of Materials Research* 99, no. 4 (April 2008): 376–380. <https://doi.org/10.3139/146.101648>
10. E. J. Pickering, H. Mathur, A. Bhowmik, O. M. D. M. Messé, J. S. Barnard, M. C. Hardy, R. Krakow, et al., "Grain-Boundary Precipitation in Allvac 718Plus," *Acta Materialia* 60, nos. 6–7 (April 2012): 2757–2769. <https://doi.org/10.1016/j.actamat.2012.01.042>
11. X. Xie, C. Xu, G. Wang, J. Dong, W.-D. Cao, and R. Kennedy, "TTT Diagram of a Newly Developed Nickel-Base Superalloy-Allvac 718Plus™," in *Superalloys 718, 625, 706 and Derivatives 2005* (Pittsburgh, PA: The Minerals, Metals, and Materials Society, 2005), 193–202.
12. R. Ebrahimi and E. Shafiei, "Mathematical Modeling of Single Peak Dynamic Recrystallization Flow Stress Curves in Metallic Alloys," in *Recrystallization* (London, UK: IntechOpen Limited, 2012).
13. S. Bao, G. Zhao, C. Yu, Q. Chang, C. Ye, and X. Mao, "Recrystallization Behavior of a Nb-Microalloyed Steel during Hot Compression," *Applied Mathematical Modelling* 35, no. 7 (July 2011): 3268–3275. <https://doi.org/10.1016/j.apm.2011.01.024>
14. M. Shaban and B. Eghbali, "Determination of Critical Conditions for Dynamic Recrystallization of a Microalloyed Steel," *Materials Science and Engineering: A* 527, nos. 16–17 (June 2010): 4320–4325. <https://doi.org/10.1016/j.msea.2010.03.086>
15. J. J. Jonas and I. Weiss, "Effect of Precipitation on Recrystallization in Microalloyed Steels," *Metal Science* 13, nos. 3–4 (March 1979): 238–245. <https://doi.org/10.1179/msc.1979.13.3-4.238>
16. G. Engberg and L. Lissel, "A Physically Based Microstructure Model for Predicting the Microstructural Evolution of a C-Mn Steel during and after Hot Deformation," *Steel Research International* 79, no. 1 (January 2008): 47–58. <https://doi.org/10.1002/srin.200806315>
17. T. Siwecki, G. Engberg, and A. Cuibe, "Thermo-Mechanical Controlled Processes for High Strength and Toughness in Heavy Plates and Strips of HSLA-Steels," in *THERMEC 97: International Conference on Thermomechanical Processing of Steels and Other Materials* (Warrendale, PA: The Minerals, Metals, and Materials Society, 1997), 757–764.
18. L. Bäcke, "Modeling the Microstructural Evolution during Hot Deformation of Microalloyed Steels" (PhD thesis, KTH Royal Institute of Technology, 2009).
19. B. Dutta and C. M. Sellars, "Effect of Composition and Process Variables on Nb(C, N) Precipitation in Niobium Microalloyed Austenite," *Materials Science and Technology* 3, no. 3 (March 1987): 197–206. <https://doi.org/10.1179/mst.1987.3.3.197>
20. B. Dutta, E. J. Palmiere, and C. M. Sellars, "Modelling the Kinetics of Strain Induced Precipitation in Nb Microalloyed Steels," *Acta Materialia* 49, no. 5 (March 2001): 785–794. [https://doi.org/10.1016/S1359-6454\(00\)00389-X](https://doi.org/10.1016/S1359-6454(00)00389-X)
21. B. Dutta and C. M. Sellars, "Strengthening of Austenite by Niobium during Hot Rolling of Microalloyed Steel," *Materials Science and Technology* 2, no. 2 (February 1986): 146–153. <https://doi.org/10.1179/mst.1986.2.2.146>
22. M. Gómez and S. F. Medina, "Role of Microalloying Elements in the Microstructure of Hot Rolled Steels," *International Journal of Materials Research* 102, no. 10 (October 2011): 1197–1207. <https://doi.org/10.3139/146.110585>
23. L. Lissel, G. Engberg, and U. Borggren, "Modeling Precipitation and Its Effect on Recrystallization during Hot Strip Rolling of Niobium Steels," in *Third International Conference on Thermomechanical Processing of Steels* (Milan, Italy: Associazione Italiana di Metallurgia, 2008), 1–12.

24. F. Tancret, E. Galindo-Nava, and P. E. J. R. Díaz-del-Castillo, "Dynamic Recrystallisation Model in Precipitation-Hardened Superalloys as a Tool for the Joint Design of Alloys and Forming Processes," *Materials & Design* 103 (August 2016): 293–299. <https://doi.org/10.1016/j.matdes.2016.04.076>
25. Y. Bergström, "A Dislocation Model for the Stress-Strain Behaviour of Polycrystalline  $\alpha$ -Fe with Special Emphasis on the Variation of the Densities of Mobile and Immobile Dislocations," *Materials Science and Engineering* 5, no. 4 (March 1970): 193–200. [https://doi.org/10.1016/0025-5416\(70\)90081-9](https://doi.org/10.1016/0025-5416(70)90081-9)
26. Y. Estrin and H. Mecking, "A Unified Phenomenological Description of Work Hardening and Creep Based on One-Parameter Models," *Acta Metallurgica* 32, no. 1 (January 1984): 57–70. [https://doi.org/10.1016/0001-6160\(84\)90202-5](https://doi.org/10.1016/0001-6160(84)90202-5)
27. D. Srinivasan, L. U. Lawless, and E. A. Ott, "Experimental Determination of TTT Diagram for Alloy 718Plus<sup>®</sup>," in *Superalloys 2012* (Hoboken, NJ: John Wiley & Sons, Inc., 2012), 759–768.
28. D. J. Bailey and W. F. Flanagan, "The Relationship between Dislocation Density and Flow Stress in Materials Deforming by a Peierls-Nabarro Mechanism," *Philosophical Magazine* 15, no. 133 (1967): 43–49. <https://doi.org/10.1080/14786436708230350>
29. M. Fisk, A. Lundbäck, J. Andersson, and L.-E. Lindgren, "Finite Element Analysis Using a Dislocation Density Based Flow Stress Model Coupled with Model for Precipitate Evolution," in *Eighth International Symposium on Superalloy 718 and Derivatives* (Hoboken, NJ: John Wiley & Sons, 2014), 155–168.
30. Y. Bergström, Y. Granbom, and D. Sterkenburg, "A Dislocation-Based Theory for the Deformation Hardening Behavior of DP Steels: Impact of Martensite Content and Ferrite Grain Size," *Journal of Metallurgy* 2010 (2010): 647198. <https://doi.org/10.1155/2010/647198>
31. B. Sonderegger, I. Holzer, E. Kozeschnik, and C. Sommitsch, "Particle Distance Distributions and Their Effect on Precipitation Strengthening," *Computer Methods in Materials Science* 11, no. 1 (2011): 148–153.
32. R. Radis, G. A. Zickler, M. Stockinger, C. Sommitsch, and E. Kozeschnik, "Interaction of the Precipitation Kinetics of  $\delta$  and  $\gamma'$  Phases in Nickel-Base Superalloy ATI Allvac<sup>®</sup> 718Plus<sup>™</sup>," *Materials Science Forum* 638–642 (2010): 2712–2717. <https://doi.org/10.4028/www.scientific.net/MSF.638-642.2712>
33. G. A. Zickler, R. Schnitzer, R. Radis, R. Hochfellner, R. Schweins, M. Stockinger, and H. Leitner, "Microstructure and Mechanical Properties of the Superalloy ATI Allvac<sup>®</sup> 718Plus<sup>™</sup>," *Materials Science and Engineering: A* 523, nos. 1–2 (October 2009): 295–303. <https://doi.org/10.1016/j.msea.2009.06.014>
34. H. J. Frost and M. F. Ashby, *Deformation-Mechanism Maps* (Oxford, UK: Pergamon Press, 1982).
35. V. Mohles, D. Rönnpagel, and E. Nembach, "Simulation of Dislocation Glide in Precipitation Hardened Materials," *Computational Materials Science* 16, nos. 1–4 (December 1999): 144–150. [https://doi.org/10.1016/S0927-0256\(99\)00056-7](https://doi.org/10.1016/S0927-0256(99)00056-7)
36. S. Mitsche, C. Sommitsch, D. Huber, M. Stockinger, and P. Poelt, "Assessment of Dynamic Softening Mechanisms in Allvac<sup>®</sup> 718Plus<sup>™</sup> by EBSD Analysis," *Materials Science and Engineering: A* 528, nos. 10–11 (April 2011): 3754–3760. <https://doi.org/10.1016/j.msea.2011.01.044>
37. D.-X. Wen, Y. C. Lin, J. Chen, X.-M. Chen, J.-L. Zhang, Y.-J. Liang, and L.-T. Li, "Work-Hardening Behaviors of Typical Solution-Treated and Aged Ni-Based Superalloys during Hot Deformation," *Journal of Alloys and Compounds* 618 (January 2015): 372–379. <https://doi.org/10.1016/j.jallcom.2014.08.187>
38. A. Najafzadeh and J. J. Jonas, "Predicting the Critical Stress for Initiation of Dynamic Recrystallization," *ISIJ International* 46, no. 11 (2006): 1679–1684. <https://doi.org/10.2355/isijinternational.46.1679>
39. P. Gong, E. J. Palmiere, and W. M. Rainforth, "Characterisation of Strain-Induced Precipitation Behaviour in Microalloyed Steels during Thermomechanical Controlled Processing," *Materials Characterization* 124 (February 2017): 83–89. <https://doi.org/10.1016/j.matchar.2016.12.009>
40. J. Andersson, G. P. Sjöberg, L. Viskari, and M. Chaturvedi, "Effect of Different Solution Heat Treatments on Hot Ductility of Superalloys Part 2 – Allvac 718Plus<sup>™</sup>," *Materials Science and Technology* 28, no. 6 (June 2012): 733–741. <https://doi.org/10.1179/1743284712Y.0000000002>
41. Y. Han and M. C. Chaturvedi, "A Study of Back Stress during Creep Deformation of a Superalloy Inconel 718," *Materials Science and Engineering* 85 (January 1987): 59–65. [https://doi.org/10.1016/0025-5416\(87\)90467-8](https://doi.org/10.1016/0025-5416(87)90467-8)
42. M. Sundaraman, P. Mukhopadhyay, and S. Banerjee, "Deformation Behaviour of  $\gamma'$  Strengthened Inconel 718," *Acta Metallurgica* 36, no. 4 (April 1988): 847–864. [https://doi.org/10.1016/0001-6160\(88\)90139-3](https://doi.org/10.1016/0001-6160(88)90139-3)
43. L. Whitmore, H. Leitner, E. Povoden-Karadeniz, R. Radis, and M. Stockinger, "Transmission Electron Microscopy of Single and Double Aged 718Plus Superalloy," *Materials Science and Engineering: A* 534 (February 2012): 413–423. <https://doi.org/10.1016/j.msea.2011.11.089>
44. M. Militzer, W. P. Sun, and J. J. Jonas, "Effect of Deformation-Induced Vacancies on Recrystallization," *Materials Science Forum* 113–115 (1993): 163–168. <https://doi.org/10.4028/www.scientific.net/MSF.113-115.163>
45. M. Condat and B. Décamps, "Shearing of  $\gamma'$  Precipitates by Single  $a/2 \langle 110 \rangle$  Matrix Dislocations in a  $\gamma/\gamma'$  Ni-Based Superalloy," *Scripta Metallurgica* 21, no. 5 (May 1987): 607–612. [https://doi.org/10.1016/0036-9748\(87\)90369-3](https://doi.org/10.1016/0036-9748(87)90369-3)
46. B. Décamps, S. Raujol, A. Coujou, F. Pettinari-Sturmel, N. Clément, D. Locq, and P. Caron, "On the Shearing Mechanism of  $\gamma'$  Precipitates by a Single  $(a/6)\langle 112 \rangle$  Shockley Partial in Ni-Based Superalloys," *Philosophical Magazine* 84, no. 1 (2004): 91–107. <https://doi.org/10.1080/14786430310001621472>
47. M. J. Whelan and P. B. Hirsch, "Electron Diffraction from Crystals Containing Stacking Faults: I," *Philosophical Magazine* 2, no. 21 (1957): 1121–1142. <https://doi.org/10.1080/14786435708242742>
48. P. Bellon, J. P. Chevalier, E. Augarde, J. P. André, and G. P. Martin, "Substrate-Driven Ordering Microstructure in  $Ga_xIn_{1-x}P$  Alloys," *Journal of Applied Physics* 66, no. 6 (September 1989): 2388–2394. <https://doi.org/10.1063/1.344245>

49. G. Van Tendeloo, O. I. Lebedev, M. Hervieu, and B. Raveau, "Structure and Microstructure of Colossal Magneto-resistant Materials," *Reports on Progress in Physics* 67, no. 8 (August 2004): 1315. <https://doi.org/10.1088/0034-4885/67/8/R01>
50. O. Skiba, A. Redjaimia, J. Dulcy, J. Ghanbaja, G. Marcos, N. Caldeira-Meulnotte, and T. Czerwiec, "A Proper Assessment of TEM Diffraction Patterns Originating from CrN Nitrides in a Ferritic Matrix," *Materials Characterization* 144 (October 2018): 671–677. <https://doi.org/10.1016/j.matchar.2018.07.019>
51. M. Gouné, A. Redjaimia, T. Belmonte, and H. Michel, "Identification and Characterization of a Novel Mn–N Nitride Formed in Fe–Mn–N Alloy," *Journal of Applied Crystallography* 36, no. 1 (February 2003): 103–108. <https://doi.org/10.1107/S0021889802020101>
52. A. Redjaimia, A. Prout, P. Donnadieu, and J. P. Morniroli, "Morphology, Crystallography and Defects of the Intermetallic  $\chi$ -Phase Precipitated in a Duplex ( $\delta + \gamma$ ) Stainless Steel," *Journal of Materials Science* 39, no. 7 (April 2004): 2371–2386. <https://doi.org/10.1023/B:JMSC.0000019999.27065.13>
53. A. Mateo, L. Llanes, M. Anglada, A. Redjaimia, and G. Metauer, "Characterization of the Intermetallic G-Phase in an AISI 329 Duplex Stainless Steel," *Journal of Materials Science* 32, no. 17 (September 1997): 4533–4540. <https://doi.org/10.1023/A:1018669217124>
54. K. Kaneko, K. Inoke, K. Sato, K. Kitawaki, H. Higashida, I. Arslan, and P. Midgley, "TEM Characterization of Ge Precipitates in an Al–1.6 at% Ge Alloy," *Ultramicroscopy* 108, no. 3 (February 2008): 210–220. <https://doi.org/10.1016/j.ultramic.2007.04.020>
55. W. Cao and G. R. Barsch, "Landau-Ginzburg Model of Interphase Boundaries in Improper Ferroelastic Perovskites of  $D_{4h}^{18}$  Symmetry," *Physical Review B* 41, no. 7 (March 1990): 4334–4348. <https://doi.org/10.1103/PhysRevB.41.4334>